The effects of particle size on reversible shear thickening of concentrated colloidal dispersions

Brent J. Maranzano and Norman J. Wagner[a]
Center for Molecular and Engineering Thermodynamics, Department of Chemical Engineering,
University of Delaware, Newark, Delaware 19716

The particle size dependence of the reversible shear thickening transition in dense colloidal suspensions is explored. Five suspensions of monodisperse silica are synthesized via the Stöber synthesis. The physicochemical properties of the dispersions are quantified using transmission electron microscopy, dynamic light scattering, small angle light scattering, electrophoresis, and viscometry. Rheology measurements indicate a critical stress marking the onset of reversible shear thickening that depends on the dispersion's particle size, concentration, polydispersity, and interparticle interactions. A simplified two particle force balance between the interparticle repulsive forces and the hydrodynamic compressive forces is used to derive a scaling relationship between this critical shear stress and the suspension properties. The scaling is tested against the fully characterized silica dispersions, which span nearly a decade in particle size. Furthermore, bimodal mixtures of the dispersions are employed to evaluate the accuracy of the scaling to predict the critical shear stress for dispersions with varying degrees of polydispersity. The success of the scaling supports the hydrocluster mechanism for shear thickening and suggests methods for controlling shear thickening by tailoring particle properties. © *2001 American Institute of Physics.*
[DOI: 10.1063/1.1373687]

I. INTRODUCTION

Colloidal dispersions in strong viscous flows can exhibit a unique transition that is characterized by a self-organization into stress-bearing clusters, often denoted by the term ''hydroclusters.'' This self-organized microstructure is thought to be a consequence of the dominance of hydrodynamic lubrication forces, whereby the flow generates transient packed clusters of particles separated from one another only by a thin solvent layer. Percolation of these hydroclusters leads to ''jamming,'' or the discontinuous, often erratic increase in shear viscosity at a critical shear stress. Evidence for the hydrodynamic basis of this phenomenon is provided by rheo-optical experiments[1,2] and stress-jump rheological measurements.[3] Simulation predictions by Brady[4] and co-workers using the method of Stokesian dynamics, and later by Boersma and co-workers[5] and Melrose and co-workers[6,7] provide computational evidence of the mechanism, whereas the statistical mechanical theory of Brady[4,8,9] provides an understanding of the microstructure resulting from the singular nature of lubrication hydrodynamics. It should be noted that there are only limited measurements of the actual stress-induced microstructure,[2,10,11] such that comparison of theory and experiment are limited at present to macroscopic rheological response. Although the basic mechanism of shear thickening is thought to be understood, detailed experimental tests that isolate the parameters controlling shear thickening are lacking.

Control of shear thickening in colloidal dispersions is also of technological relevance for numerous industrial products such as paints, lubricants, pharmaceutical, and micro-abrasives that are often processed at high shear rates and stresses. Improving the performance of these materials often requires delicate tailoring of the physicochemical properties of the dispersions. Consequently, alterations in the particle's properties may require new processing conditions, or risk the possibility of encountering shear thickening, which can cause equipment damage and failure, as well as irreversible aggregation of the dispersion.

The relationship between particle properties in a dispersion to shear thickening has been the subject in numerous investigations.[1,5,9,12–19] A review of shear thickening by Barnes[16] summarizes the various suspended phase parameters influencing shear thickening: particle size, polydispersity, shape, and interactions, as well as the properties of the continuous phase. In the review, Barnes regressed shear thickening data reported in the literature to determine that the critical shear rate for shear thickening scaled as the inverse of the particle radius squared. However, in drawing this conclusion he did not consider the underlying microstructural changes that facilitated shear thickening. Alternatively, Hoffman[19,20] presented a physical model for shear thickening based on the balance between interparticle and shear forces. In deriving the relationship, he surmised shear thickening occurred when lubrication forces between neighboring particles in a highly organized, layered flow induced particles to rotate out of alignment and destabilized the flow (denoted as an order–disorder transition). Later, Boersma *et al.*[5] furthered Hoffman's[19] approach and simplified the force balance to render a dimensionless critical shear rate, which was

used to correlate the shear thickening from a number of dispersions. In their model[5,19] shear thickening occurs when hydrodynamic lubrication forces exceed interparticle forces, which destabilizes particles flowing in a layered structure and results in an increase in viscosity due to increased interparticle interactions.

Boersma and co-workers evaluated their model for predicting the onset of shear thickening against six dispersions of various particle types, sizes, and polydispersities. However, because the dispersions lacked congruency, they were not able to systematically isolate and investigate the effects of each parameter independently. Further, their analysis focused on electrostatic forces while neglecting van der Waals and Brownian forces, which may have contributed substantially to the overall interparticle interactions for some of the dispersions investigated. Finally, the premise that shear thickening necessarily occurs from an order to disorder transition has been refuted by measurements of the microstructure change accompanying shear thickening, which supports the mechanism first suggested by the Stokesian dynamics simulations of Bossis and Brady[4,8,21] as verified by others[6,22,23] that shear thickening results from the formation of a nonequilibrium, self-organized microstructure that develops under strong flows, denoted as ''hydroclusters.''

SANS measurements of the shear induced microstructure[10,11,13,15,24–26] and associated rheo-optical[1,2,13] and stress-jump measurements[27] demonstrated that shear thickening is a consequence of greatly increased lubrication stresses associated with the hydrocluster formation. Bender and Wagner[13] translated the concept of hydrocluster formation as the mechanism of reversible shear thickening into predictions of a critical stress for shear thickening by explicitly considering the balance between interparticle and hydrodynamic forces acting between two particles. A mean field correction was introduced to account for the added hydrodynamic forces associated with the finite particle concentration. This resulted in predictions of a critical stress for the onset of shear thickening that was successful in predicting the behavior of concentrated, hard-sphere dispersions.

Chow and Zukoski[15,24] were able to partially scale the shear rates at which their model, charge stabilized suspensions shear thickened by a characteristic time given by the ratio of the solvent viscosity to the suspension's static elastic modulus (the suspensions exhibited apparent yield stresses). It was postulated that if the shear rates exceed the time required for density fluctuations to relax, which is proportional to this characteristic time, stress fluctuations cannot relax and shear thickening is induced. The fact that shear thickening was not observed in their systems for volume fractions below 50% was rationalized by arguing that particle diffusion is reduced at higher concentrations and that the relaxation of the fluctuations is proportional to this self-diffusivity and the characteristic time. This argument introduced the concept of a competition between time scales that has been recently expanded upon and quantified by Melrose and co-workers.[6,23] They postulated an additional criterion for shear thickening, relating the critical shear rate to the characteristic relaxation time of a particle doublet. The argument is a competition of time scales for convection due to shear vs

the time required for a doublet to decouple due to repulsive interparticle forces. In their analysis the rate at which a doublet separates is determined by the ratio of the hydrodynamic drag to the effective spring constant of the interparticle interaction calculated at a characteristic separation distance. This separation distance is given by a force balance similar to that used by Boersma et al.[5] and Bender and Wagner,[13] who balanced the hydrodynamic and interparticle forces. Although not predictive as presented, the resulting criterion was able to rationalize the results of their restricted Stokesian dynamics simulations.

The simulations underlying these arguments have been preformed primarily on near or actual hard sphere systems. A key issue in the simulations is resolving the details of the hydrodynamic interactions for particles in close approach,[6,28] such that mathematically smooth hard-spheres actually ''jam'' and cannot flow. A consequence of the extensive simulation work is that the detailed behavior of a shear thickening system is known to be extremely sensitive to the details of the interparticle forces and hydrodynamic properties of the particles on the level of the surface roughness (i.e., angstroms to nanometers). Nearly, but not all, of the previous work has investigated polymeric or oxide dispersions with grafted or adsorbed surfactant, leading to substantial uncertainty about these forces on this length scale. Further, dispersion forces will be substantial for systems that are not index matched, and the role of the attractive interactions on the onset and mechanism of shear thickening has not been established. Thus to compare better with the current level of theoretical understanding, a model system of stable, smooth, chemically homogeneous, monodisperse, and index matched particles covering a broad range of sizes with tunable surface properties is required. Previous work with coated Stöber silica particles[2,13,27,29–31] suggest this as a nearly optimal system for further investigation.

In this work, we explore the effects of particle size and concentration on reversible shear thickening by performing rheological measurements on a set of chemically similar, nearly monodisperse Stöber silica dispersions that span nearly a decade in particle size. A silane coupling agent is used to neutralize nearly all of the surface charge and enable dispersing the particles in an index matching solvent. The effects of particle polydispersity are tested with bimodal dispersions created from combinations of the former suspensions. The measurements are used to critically test the aforementioned scaling predictions for the onset of shear thickening and an improved, predictive method for determining the onset of shear thickening is presented.

II. METHODOLOGY

A set of chemically analogous dispersions are synthesized via the Stöber synthesis,[29–31] where seeded growth is used to vary particle size. The reaction is terminated by adding a stoichiometric quantity of a silane coupling agent, 3-(trimethoxysilyl) propyl methacrylate (TPM), which eliminates most (>99%), but not all, of the surface silanol groups.[29,32] The particles are resuspended in an index matched organic solvent, tetrahydrofurfuryl alcohol (reagent

grade Aldrich, $\rho = 1.054$ g/cm^3, $n_D^{20} = 1.4512$, $\mu = 5.44$ cP), by repetitive centrifugation and suspending. The matching of the refractive indices minimizes the attractive dispersion forces, such that the resulting suspensions are weakly charge-stabilized and can be considered near hard-sphere dispersions.

Full characterization of the particle size, polydispersity, density, and surface charge is required to unambiguously test models for the shear thickening transition. Particle size distributions (PSD) are measured and verified using transmission electron microscopy (TEM), dynamic light scattering (DLS), and small angle neutron scattering (SANS). TEM measurements consist of imaging a minimum of 200 particles per suspension with a Philips 400 electron microscope calibrated against a 0.5 μm diffraction grating coated with 261 nm polystyrene beads. The particle diameter is determined by averaging the major and minor ellipsoidal axis, as well as calculating it from the measured area using $d = \sqrt{(4\text{Area}/\pi)}$. DLS experiments consist of measuring the characteristic decay time (Γ^{-1}) of the intensity autocorrelation function as a function of wave vector (q) at three solids concentrations for each suspension to insure that the infinite dilution approximation is valid. The decay time yields the diffusion coefficients as $\Gamma = D_O q^2 + \Theta_O$, where Θ_O is the rotational diffusivity and D_O is the bare particle translational diffusivity given by $D_O = (k_B T / 6\pi\mu a)$ from which the particle radius, a, is determined.

For small particles (<300 nm), SANS provides another measure of the PSD. The experiments and analyses are described in detail in Ref. 32. The particle size and polydispersity are determined from fitting data obtained from dilute dispersions, whereas the interaction potential is obtained from scattering from more concentrated dispersions. SANS measurements for concentrated solutions, such that $S(q) \neq 1$, can be used within the context of DLVO theory to extract the surface potential and Debye screening length, as described previously.[32,33] Index matching minimizes van der Waals interactions, so only electrostatic interactions and hard-core excluded volume effects are considered.

Particle densities are estimated by dilution viscometry and solution densitometry measurements. Past investigations using Stöber silica suggest a particle microporosity[34–36] that may be a function of particle size,[31] which leads to a lower apparent particle density than the SiO$_2$ density. Others, however, report better correlations in viscometry measurements using a nonmicroporous estimate for the particle density.[37] Here, the SiO$_2$ density is calculated from solution (THFFA) densitometry measurements at various solids weight fractions using a volumetric balance assuming ideal mixing.[38] Weight fractions are determined from measuring the remaining powder mass after drying the samples at 130 °C for at least 8 h. Measurements of the weight fraction for drying times longer than 8 h showed no changes.

The hydrodynamic particle density is determined from low concentration zero shear viscometry data, where the zero shear viscosity can be approximated as a Taylor series expansion in volume fraction. The apparent particle density, ρ_{particle}, is then extracted by comparing the measured intrinsic viscosity $[\eta]$ with the dilute limiting value for spherical particles (2.5) derived by Einstein. Dilution viscometry experiments also provide an indication of the interparticle interactions through the Huggins coefficient, κ_H. Deviations in the Huggins coefficient from a hard sphere value of $\kappa_H \approx 1$ (Refs. 39, 40) can be attributed to residual charges from unreacted silanol groups on the surface of the particle.[29,31] Estimates of the charge can be made from electrophoresis experiments, but previously have been limited to solutions in polar solvents.[29,31] Similar measurements in organic solvents, such as THFFA, have been difficult because of the low silanol dissociation.[29] Here, we exploit the increased sensitivity of a heterodyne Zeta PALS instrument to measure the particle mobilities directly in the THFFA solvent. The mobilities, ν, are then converted to zeta potentials, ζ, using the Hückel equation, which serve as approximations for the surface potential, ψ_s. Measurements spanning a range of concentrations and voltages verify that the zeta potential values are independent of the applied voltage and concentration within the range of the investigation.

The rheological measurements are conducted on a Bohlin CS controlled stress rheometer. The rheometer has a torque range of 0.001–10 mNm with a torque resolution of 0.0002 mNm and an angular deflection resolution of 1.6 μrad. The data reported here is produced with several tools and geometries including: 40 mm-4°, 40 mm-1°, 20 mm-4°, and 20 mm-1° cone and plates. Additional tests with a 20 mm parallel plate and a Couette cell (DIN 25 mm) verified that the results are independent of geometry. Previous investigations on the rheology of concentrated dispersions have shown that the shear history can have a profound impact on the experiments. Therefore, the following protocol is strictly adhered to for all measurements:

(1) A 3 min stress ramp from 0.1 Pa to 4700 Pa to remove shear history effects;
(2) A 2 min creep experiment at a shear rate of 1 s^{-1} followed by 30 s recovery;
(3) A stress sweep from 0.5 Pa to 4700 Pa obtaining 20 logarithmically spaced points. The sample was allowed to equilibrate for 10 s before each stress measurement followed by averaging the viscosity response for 20 s. Note: The maximum stress for dilute suspensions was dictated by centrifugal forces.
(4) A stress sweep from 0.06 Pa to 10 Pa with 1 min equilibration and 2 min averaging.
(5) A stress sweep near the critical shear stress collecting 30 points with 10 s equilibration and 20 s averaging.
(6) A frequency sweep from 0.1 to 100 Hz at 1% strain.
(7) A 2 min creep experiment at a shear rate of 1 s^{-1} followed by 30 s recovery.

Data sets that exhibited substantial differences between the first and last creep experiments, which were thought to be due to drying effects, were rejected and a new sample was tested.

The transition to the shear thickening regime for very small particle sizes can occur at high shear rates, where the onset of secondary flows is a concern. We model the secondary flow effects for each tooling using rheological data from

Newtonian silicone oils fit to the following scaling relationship:[41]

$$\tau = \tau_0 (1 + \lambda \, \mathrm{Re}^2). \tag{1}$$

Here, τ is the apparent shear stress, τ_O is the stress without secondary flows, Re is the Reynolds number ($= \rho \Omega \beta^2 R^2 / \eta_0$), and λ is a tool specific parameter that is evaluated separately for each cone ($\lambda = 20{:}20$ mm-1°, 400: 40 mm-1°, 0.25: 20 mm-4°, 3: 40 mm-4°). The model is subsequently used to subtract viscosity increases attributed to energy dissipated in secondary flows as predicted by Eq. (1).

Past investigations have reported critical stress values marking shear thickening that vary with rheometer gap thickness.[24] We verify that the critical stress values reported here are independent of gap thickness through measurements of individual sample loadings using 20 mm parallel plates where the gap size is varied from 1000 μm to 20 μm. This experimental data was also used to determine the slip velocities at various applied stress levels.[42] Further, the rheology was verified to be independent of the measurement technique by successful comparison of measurements for both the HS1000 and HS600 dispersions at several concentrations obtained on a RMS 800 rate controlled rheometer with those obtained on the Bohlin CS rheometer.

We exploit the sensitivity of the zero shear viscosity to interparticle interactions to the weak electrostatic interactions arising from residual surface charges. At high concentrations where the samples show evidence of an apparent yield stress, "zero shear" viscosities are extracted from our measurements by the method proposed by Russel and Grant.[43] The measurements at low stress are plotted according to[44]

$$\tau = K \dot{\gamma}^{0.5} + \tau_{\mathrm{yield}} \tag{2}$$

and extrapolated to zero shear rate to determine the apparent yield stress τ_{yield}. Congruence from measurements on multiple instruments and tooling demonstrates we are measuring yielding and not slip. The zero shear viscosity is obtained by subtracting this yield stress from the measured stress and averaging the resultant low shear viscosities.

For dilute dispersions the zero shear viscosities are determined directly from Ubbelhode viscometry measurements. These data sets are combined to yield the dependence of the zero shear viscosity on volume fraction. This information can be used to gauge the influence of the residual, weak electrostatic interactions on the rheology through consideration of the effective hard-sphere particle volume that yields the equivalent viscosity as the measured suspension.[33,45] Electrostatic repulsions lead to an effective hard-sphere radius greater than the actual core and thus, decrease the maximum packing fraction of the dispersion. An empirical relation can be used to model this increase:

$$\phi_{\mathrm{effective}} = \phi \left(1 + \frac{\alpha}{\kappa a} \right)^3. \tag{3}$$

The parameter α is obtained from matching the maximum packing fraction to that for hard spheres, which is taken to be 0.58.[46] The maximum packing fraction is obtained by fitting the zero shear viscosity data to the Krieger–Dougherty relationship[47] [Eq. (4)] using $\phi_{\max}$ as an adjustable fitting parameter,

$$\eta / \mu = \left(1 - \frac{\phi}{\phi_{\max}} \right)^{2.5 \phi_{\max}}. \tag{4}$$

III. THEORY: SCALING FOR THE ONSET OF SHEAR THICKENING

The "critical" shear stress, viscosity, and shear rate at the shear thickening point are determined by fitting the double logarithmic plots of viscosity vs shear stress (both ascending and descending data) for each suspension to a quadratic curve. The "critical stress" τ_c is defined to be the stress at the minimum, and the "critical shear rate" $\dot{\gamma}_c$ calculated from the "critical shear viscosity" η_c and τ_c. These parameters are taken to mark the onset of shear thickening, although the initial formation of hydroclusters in the shearing dispersion may precede this upturn in shear viscosity.[13] These parameters are used to test the following scaling arguments for the onset of shear thickening.

The scalings derived from force balances assume a characteristic separation between particles. Two particles are placed in the plane of shear oriented along the compression axis and the forces driving particles together are balanced against the repulsive forces due to interparticle (i.e., electrostatic or steric) potentials and Brownian motion. The scaling for hard spheres proposed by Bender and Wagner[13] defines a dimensionless critical shear stress by taking the ratio of the lubrication hydrodynamic force, with a mean-field correction for the suspension viscosity, to the Brownian force [Eq. (5)],

$$
\begin{aligned}
\tau_{\mathrm{cr}}^{\mathrm{Br}} = \frac{F_{\mathrm{hydrodynamic}}(\tau_c)}{F_{\mathrm{Brownian}}} &= \frac{3 \pi \mu a^3 \dot{\gamma}_c / 2h}{-k_B T \left. \dfrac{\partial \ln g(r)}{\partial r} \right|_{r = 2a + h}} \left(\frac{\eta_c}{\mu} \right) \\
&= \frac{3 \pi \tau a^3 / 2h}{-k_B T \left. \dfrac{\partial \ln g(r)}{\partial r} \right|_{r = 2a + h}}.
\end{aligned} \tag{5}
$$

Here, μ is the solvent viscosity, k_B is Boltzmann's constant, T is absolute temperature, $g(r)$ is the equilibrium pair distribution function, which is a function of center to center separation distance (r), and τ_c, $\dot{\gamma}_c$, and η_c are the shear stress, shear rate, and viscosity, respectively, at the shear thickening point. Some details of this derivation and the basis for the mean-field correction are given in the Appendix.

In the above expression the forces are evaluated at the characteristic separation distance of the particle surfaces $h = r - 2a$ given by the following expression:[5,13]

$$\frac{h}{a} = 2 \left[\left(\frac{0.71}{\phi} \right)^{1/3} - 1 \right]. \tag{6}$$

This scaling for the average separation is derived by dispersions with liquidlike structure, which can flow with a maxi-

mum packing fraction of 0.71, as reported by de Kruif et al.[35] Other choices are appropriate for ordered disperson.[5]

τ_{cr}^{Br} is expected to be of order one at the onset of reversible shear thickening. This scaling is derived by exploiting the fact that shear thickening is driven by the onset of hydrocluster formation, which itself is a consequence of the dominance of shear driven lubrication forces over all other colloidal forces (assumed by Bender and Wagner to be Brownian motion). Notice that for hard sphere dispersions, this approach predicts the critical stress for shear thickening, τ_c^{Br}, should scale inversely with particle size cubed.

This approach can be readily extended to charge stabilized dispersions by appropriate inclusion of the electrostatic repulsive force in the balance. Boersma et al.[5] considered non-Brownian, micron-sized dispersions dominated by strong electrostatic stabilization. As per Boersma et al., we take as a characteristic value of the electrostatic force that obtained from the linearized Derjaguin approximation of the solution of the Poisson–Boltzmann equation[48] for the constant potential, evaluated at the particle surface. Taking the ratio of the hydrodynamic force between two isolated spheres to the electrostatic force at contact yields a dimensionless critical shear rate in the form of a Peclet number,

$$Pe_{cr}^{elec} = \frac{F_{hydrodynamic}(\dot{\gamma}_c)}{F_{electrostatic}(h\rightarrow 0)} = \frac{3\pi\mu a^3 \dot{\gamma}_c/2h}{2\pi\epsilon_0\epsilon_r\psi_s^2\kappa a/2}. \quad (7)$$

Note that Boersma et al. proposed a similar scaling, which differs only in the numerical prefactor, from considering Hoffman's proposed order–disorder mechanism.

The mean-field correction can be applied to this scaling to yield a critical stress prediction as

$$\tau_{cr}^{elec} = \frac{3\pi\tau_c a^3/2h}{2\pi\epsilon_0\epsilon_r\psi_s^2\kappa a/2}. \quad (8)$$

Although the size dependence is not as obvious as that obtained for hard-spheres, analysis of the expression for reasonable values of the surface charge and solution ionic strengths typical of concentrated, highly charged, stable dispersions suggests the critical stress (or shear rate) scales roughly inversely with particle size.[5]

Explicit consideration of the dynamics of hydrocluster formation by Melrose and Ball[23] leads to the specification of a characteristic relaxation time for a particle pair to "decouple." Hydroclusters are expected to grow only when this relaxation time is greater than the characteristic time for convection, which scales inversely with the applied shear rate. In this manner, the hydrocluster cannot be driven apart by the interparticle forces before being "recompressed" by the applied flow.

The lifetime of a doublet, which is a taken as characteristic of the hydrocluster, is given by the ratio of the interparticle hydrodynamic resistance coefficient, $\alpha(h_m)$, to the "effective spring constant" between particles, $K(h_m) = dF(h)/dh|_{h=h_m}$, evaluated at a characteristic particle separation, h_m. The interparticle resistance coefficient is given by

$$\alpha(h_m) = \frac{3\pi\mu a^2}{2h_m}. \quad (9)$$

The effective spring constant for electrostatically stabilized particles is given by the derivative of the nonlinear electrostatic force acting between charged colloids[48] (with constant surface potential),

$$K(h_m) = \frac{d}{dh}F_{electrostatic}(h)|_{h=h_m}$$

$$= 2\pi\epsilon_0\epsilon_r\psi_s^2\kappa^2 a\left(\frac{e^{-\kappa h_m}}{(1+e^{-\kappa h_m})^2}\right). \quad (10)$$

In the above, ϵ_0 is the permittivity of the vacuum and ϵ_r is the permittivity of the solvent. Thus, the scaling proposed by Melrose and Ball[23] predicts shear thickening will occur when $\dot{\gamma}[\alpha(h_m)/K(h_m)]>1$. From this, a dimensionless critical shear rate is derived as a Peclet number,

$$Pe_{cr}^M = \frac{3\pi\mu\dot{\gamma}_c a^2/2h_m}{2\pi\epsilon_0\epsilon_r\psi_s^2\kappa^2 a\dfrac{e^{-\kappa h_m}}{(1+e^{-\kappa h_m})^2}}. \quad (11)$$

The above equations are to be evaluated at the characteristic interparticle separation distance at the point of shear thickening. Unlike the previous approaches where this distance is specified geometrically, the characteristic separation distance, h_m, is set by the balance between the shear forces and the repulsive electrostatic forces. The shearing force driving the particle pair together is taken to scale as the applied stress times the cross sectional area, which is estimated by the particle diameter squared, while the same nonlinear electrostatic repulsion is assumed to be the dominate repulsive force. This leads to the following expression that is to be solved for h_m by taking the applied stress at the point of shear thickening (the critical stress) as

$$\tau_c 4a^2 = 2\pi\epsilon_0\epsilon_r\psi_s^2\frac{\kappa a e^{-\kappa h_m}}{1+e^{-\kappa h_m}}. \quad (12)$$

Melrose was able to verify the validity of the above approach by rationalizing the results of his restricted Stokesian Dynamics simulations. These simulations, however, neglected many-body hydrodynamic interactions. The dominant effect of these interactions would be to further retard the rate at which a particle pair in close proximity relaxes (i.e., to stablize the hydrocluster structure). Using the concepts of hydrodynamic preaveraging,[45,49–51] this effect can be accounted for to first order by replacing the solvent viscosity in the expression for $\alpha(h)$ with the suspension's hydrodynamic viscosity. Further, commensurate with the approximations of Bender and Wagner, the product of hydrodynamic viscosity and shear rate can be taken to be the actual applied stress. With this mean-field hydrodynamic correction, Eq. (11) takes the form of a reduced critical stress for shear thickening:

$$\tau_{cr}^M = \frac{3\pi\tau_c a^2/2h_m}{2\pi\epsilon_0\epsilon_r\psi_s^2\kappa^2 a\dfrac{e^{-\kappa h_m}}{(1+e^{-\kappa h_m})^2}}. \quad (13)$$

Note that this correction is already inherent in the determination of the mean particle separation [h_m, Eq. (12)] through the direct use of the critical stress τ_c in the force balance.
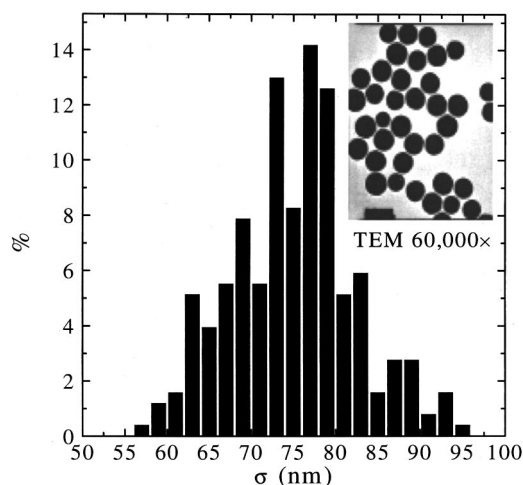
FIG. 1. Particle size distribution histogram for the HS75 dispersion obtained from TEM measurements. The inset shows a photograph obtained from TEM measurements at a magnification of 60 000.

The size scaling in the above balances is nontrivial as the surface potential and suspension ionic strength may depend on particle size. However, as will be shown, for the concentrated suspensions considered here, these balances yield critical shear rates and stresses that scale approximately inversely with particle size squared.

Finally, we note that the analysis presented by Melrose and Ball was not predictive as the measured critical stress was required to calculate the characteristic separation distance. However, with the mean-field correction, the equation for the critical stress [Eq. (13)] can be used with the force balance [Eq. (12)] to determine both the critical stress and separation distance simultaneously for a well characterized dispersion. This enables the method to be predictive, as follows.

Setting $\tau_{cr}^M = 1$ in Eq. (13) and substituting τ_c from Eq. (12) leads to a relation for the characteristic separation distance h_m in the incipient hydrocluster state, which is observed to only depend directly upon κ^{-1}, the Debye length. However, for samples without significant added electrolyte, the counterion concentration and hence, the Debye length, will depend on the surface charge density, particle size, and

particle concentration. The solution of this equation is $\kappa h_m = 1.453$, which when substituted into Eq. (12) yields

$$\tau_c = 0.024 \frac{k_B T (\kappa a) \Psi_s^2}{a^2 l_b}, \tag{14}$$

where l_b is the Bjerrum length defined by $l_b \equiv e^2/(4\pi\epsilon\epsilon_0 k_B T)$, and $\Psi_s = \psi_s e/k_B T$ is the dimensionless surface potential. For a series of suspensions where $(\kappa a)\Psi_s^2 \approx$ constant, the critical stress would scale inversely with the particle surface area $\approx a^{-2}$. However, the model suggests that a more complex size and concentration scaling may be observed due to the size dependence of κ and Ψ_s.

IV. RESULTS

The particles are observed to be nearly monodisperse, spherical and well dispersed in THFFA. The inset in Fig. 1 shows a TEM image of the HS75 dispersion, with the accompanying particle size distribution (PSD) histogram. The number average diameter obtained from the TEM analysis is 75.0 ± 7.3 nm corresponding to a polydispersity of 9.7%. The results of the sizing analysis as well as the other characterization measurements are summarized in Table I. Table I shows that the particle diameters determined from DLS measurements typically range from 5% to 25% larger than the particle diameters determined from TEM measurements. This is a consequence of the intensity squared weighted distribution obtained from DLS measurements, as compared to the number weighted particle diameter obtained from TEM experiments. For the smaller particles within the range of sizes accessible by SANS, the measured diameters obtained from fitting the form factors measured in dilute dispersions are close to the TEM measured diameters, as are the particle polydispersities. The ratio of the major to minor ellipsoidal axes (a/b) obtained from TEM experiments indicate the particles are spherical, which is further supported by the negligibly small rotational diffusion coefficients determined from DLS experiments.

The zeta potentials measured by electrophoresis measurements range from -42 mV to -90 mV, which in terms of a dimensionless potential ($\zeta e/k_B T$) range from -1.5 to -3.3. As reported in Ref. 32, SANS spectra from concentrated dispersions of HS75 can be successfully fit with a

TABLE I. Particle characterization summary.

	HS75	HS150	HS300	HS600	HS1000
σ_{TEM} (nm)	75 ± 7.3	167.3 ± 14.8	302.0 ± 26.2	608.6 ± 80.8	656.4 ± 64.3
σ_{DLS} (nm)	88.8 ± 0.8	177.8 ± 4.1	330.7 ± 19.5	633.1 ± 114.4	845.5 ± 184.8
σ_{SANS} (nm)	71.0 ± 7.0	162.0 ± 14.3	318.0 ± 16.7		
a/b	1.07 ± 0.06	1.04 ± 0.03	1.03 ± 0.02	1.04 ± 0.1	1.03 ± 0.04
Θ_0 (s^{-1})	-100.5 ± 1.0	-2.94 ± 7.6	2.92 ± 14.1	60.4 ± 5.9	8.2 ± 68.6
ζ (mV)	-42.6 ± 4.7	-72.1 ± 5.3	-42.3 ± 7.5	-92.7 ± 13.1	-68.2 ± 6.5
$\kappa a(\phi=0.5)$	13.2 ± 1.3	28.5 ± 2.5	41.7 ± 3.62	87.1 ± 11.6	89.9 ± 8.8
ϕ_{max}	0.38	0.38	0.46	0.52	0.51
α	1.8	3.9	3.3	3.2	3.9
κ_H	3.78 ± 1.24	2.28 ± 1.24	$0.61 \pm .93$	1.18 ± 2.46	3.6 ± 1.24
ρ_{SiO_2} (g/cm^3)	1.70 ± 0.01	1.90 ± 0.01	1.82 ± 0.01	1.85 ± 0.01	1.76 ± 0.04
$\rho_{particle}$ (g/cm^3)	1.45 ± 0.02	2.16 ± 0.02	1.82 ± 0.08	1.87 ± 0.13	1.77 ± 0.10

Yukawa potential using the measured zeta potential as the surface potential. A hard-sphere potential fails to adequately describe the structure factor of the dispersion. The SANS and the Zeta PALS measurements quantify that in excess of 98% of the surface silanol groups were reacted with the silane coupling agent TPM upon coating.[32] Further quantitative verification of the particle homogeneity, size, polydispersity, and surface potential was achieved by applying the GIFT approach of Glatter.[32,52]

Brownian and dispersion forces comprise the remaining thermodynamic forces in these dispersions. The index matching of the particles to the solvent minimizes the van der Waals interactions compared to the Brownian and electrostatic interactions. Further evidence that the particles are not simply hard spheres is indicated by the deviation in the Huggins coefficients from the hard sphere value of $\kappa_H \approx 1$.[39,40] The Huggins coefficients for these dispersions average slightly over 2, due to weak, short-range electrostatic interactions from unreacted silanol groups.

SANS measurements were also performed in the NIST Couette shear cell and will be reported in detail elsewhere.[53] Extensive investigations of both radial (on) and tangential (off) axis scattering demonstrated unequivocally,[20] in agreement with our previous measurements[13] on these systems as well as those of others on similar systems,[10] that the samples do not order and that no order–disorder transition accompanies shear thickening.

Table I also compares the density of SiO_2 determined from gravimetric density measurements to the hydrodynamic particle density determined from dilution viscometry experiments. A hydrodynamic particle density substantially less than the density of amorphous SiO_2 suggests particle porosity, which has been reported by some authors[34–36] who obtain particle densities of approximately 1.65 g/cm^3. Here, the particle densities from solution densitometry (1.81 ± 0.08 g/cm^3) are comparable to results reported by Rueb and Zukoski[37] (1.8 ± 0.05 g/cm^3), who found better rheological correlations using the gravimetric density. NMR spectroscopy provides evidence that the silica is not a fully condensed SiO_2 network, thus supporting microporosity,[29–31,54] but suggests that these micropores are inaccessible for solvent penetration.[31] Thus, the hydrodynamic and gravimetric densities should be similar, but lower than amorphous bulk silica (2.2 g/cm^3). Throughout our work we use a gravimetric density for converting weight fractions into volume fraction.

The shear rheology of all our dispersions exhibited highly reversible (i.e., little or no hysteresis), shear thinning flow curves with reversible shear thickening at higher shear rates and particle loadings. The reversibility of the transition and the time response is evident in Fig. 2, which compares data for stress and rate jumps into the shear thickening regime taken on controlled stress and controlled rate rheometers, respectively.

The shear thickening is reversible, and the response time is observed to be faster than our data acquisition time (ms). Further, under controlled stress conditions, the sample can be studied at a steady, shear thickened state. Under controlled rate conditions, the behavior in the shear thickening state becomes erratic and if sheared long enough, the sample is
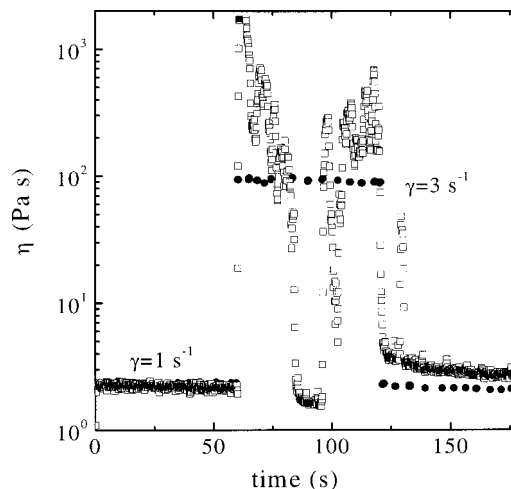

FIG. 2. (●) Stress jump measurement from $\dot{\gamma}=1$ s^{-1} (below critical shear thickening stress) to $\dot{\gamma}=3$ s^{-1} (above critical shear thickening stress) then returning to $\dot{\gamma}=1$ s^{-1} on the HS1000 dispersion at $\phi=0.53$ with a Bohlin CS rheometer. (□, filled) Rate jump performed on the same dispersion from $\dot{\gamma}=1$ s^{-1} to $\dot{\gamma}=3$ s^{-1} and back performed on an RMS-800 controlled rate rheometer.

observed to fracture and fail. This observation provides evidence for the "jamming" observed in the simulations of Melrose and co-workers.[6]

Figure 3 shows a representative example of viscosity curves at various volume fractions obtained on a controlled stress rheometer. The viscosity of the solvent THFFA at 20 °C is 5.44 cP for reference. In the shear thickening regime each flow curve consists of an up and down sweep in stress with minimal hysteresis. At low and intermediate particle concentrations ($\phi \leq 0.49$) the viscosity increases smoothly into the shear thickening region. However, at higher solids loadings, the viscosity curve at the shear thickening transition becomes discontinuous. In all cases the shear thickening transition is reversible with little or no observable hysteresis and no particle aggregation.
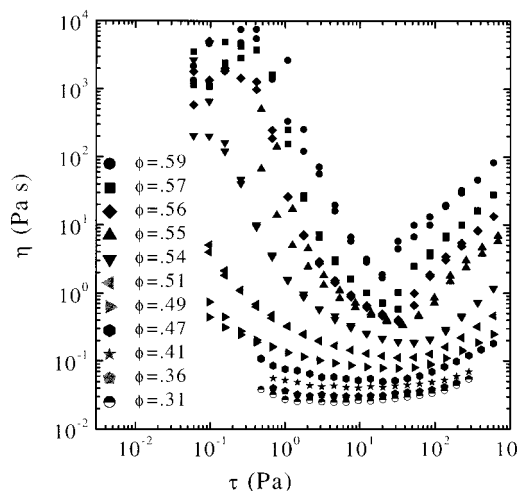

FIG. 3. Steady state viscosity curves measured with cone and plate geometry on a Bohlin CS controlled stress rheometer for the HS600 dispersion at various volume fractions as indicated. The curves for $\phi \geq 0.49$ are comprised of both ascending and descending stresses to illustrate the lack of hysteresis.
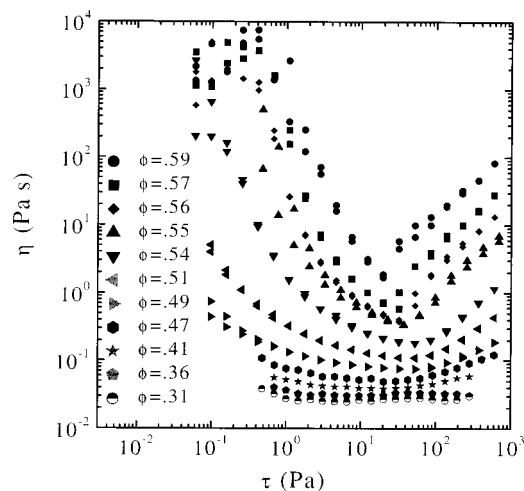
FIG. 4. Viscosity curves shown in Fig. 3 corrected for secondary flows according to Eq. (1).
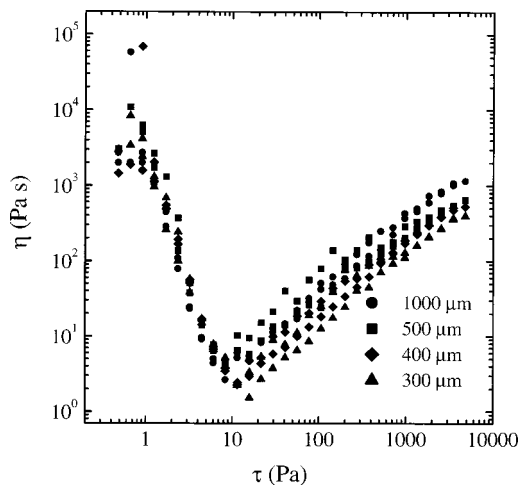

FIG. 5. Viscosity curves measured with a 20 mm parallel plate geometry on a Bohlin CS50 controlled stress rheometer for the HS300 dispersions at $\phi = 0.50$ with various rheometer gap sizes.

Previous studies suggest that there may be a lowest volume fraction below which shear thickening does not occur,[16,24] whereas theory[55] and simulation[9,21,56] demonstrate that shear thickening occurs even for dilute suspensions, but that the viscosity increases only logarithmically with the applied shear rate. Note that in Fig. 3 the lowest concentrations ($\phi < 0.41$) appear to weakly shear thicken, but an analysis of the secondary flows indicates that the small increase in viscosity may be an artifact. The corresponding viscosity curves corrected for secondary flows according to Eq. (1) are replotted in Fig. 4. In performing this correction, the viscosity at the minimum in the flow curve is used to calculate the Reynolds's number and the value of λ is taken to be that obtained on a comparable Newtonian oil. The corrected viscosity data at high solids concentrations show no significant change from the uncorrected data. Contrarily, the correction of viscosity data at low concentrations ($\phi \leqslant 0.41$) and large shear stresses indicates that secondary flows, which causes an erroneously higher viscosity, impedes accurate assessment of the critical shear stress for dilute dispersions with weak shear thickening. For these dispersions, rheo-optical techniques may supply a better method for extracting the critical point for shear thickening.[1,2] Thus, reducing the volume fraction results in a transition from discontinuous shear thickening to a less extreme shear thickening, but instrument limitations prevent definitive determination of a critical volume fraction below which shear thickening occurs. Similar results were obtained for all of the dispersions of other particle sizes.

Another difficulty in defining a critical shear stress for shear thickening has been reported in investigations where the critical stress varies with rheometer gap thickness.[24] Figure 5 shows a set of viscosity curves for the HS300 dispersion at $\phi = 0.5$ and various gap sizes, all of which are significantly larger than the particle size. The data are typical of extreme shear thickening samples, where increases in shear stress in the shear thickening regime result in increases in viscosity, but not in shear rate. Although the low shear rheology remains essentially independent of gap size, the viscosity in the shear thickening regime systematically de-

creases with decreasing gap size. Notice, however, that the shear stress at the onset of shear thickening remains nearly constant ($\tau_c \approx 10 \, \text{Pa}$) over the range of gap sizes shown. Experiments conducted on a lesser concentrated sample of the HS300 dispersion ($\phi = 0.45$) show no dependence of the critical stress on the gap sizes for gaps as low as 20 μm. Further decreases in the gap size below 20 μm lead to the occurrence of a yield stress in the dispersion. The yield stress may be due to a percolated microstructure that completely spans the rheometer tooling at the smaller gap sizes, similar to that observed in other systems.[24]

Standard analysis of the slip velocity and slip length,[57,58] that account for non-Newtonian fluid effects, are performed on the data presented in Fig. 5. Plots of the apparent measured shear rate at constant plate edge stress vs the inverse of the gap yield measures of the slip velocity and the true shear rate. Calibration of the method and instrument with a 5 Pa s silione oil yielded a slip length of $58.9 \pm 0.9 \, \mu$m, in good agreement with expectation based on a molecular slip layer.[58]

For the colloidal fluids tested here in the shear *thinning* regime the slip length and slip velocity can not be resolved within experimental measurement uncertainty. This is consistent with the slip length being on the order of the colloidal size. Contrarily, during shear thickening substantial slip is observed such that the analysis yields true shear rates that are only a few percent of the apparent shear rate. The resultant slip lengths are, to within uncertainty, the size of the gap. Thus, we conclude that for the discontinuous shear thickening samples, in the shear thickening regime the sample solidifies and does not flow. This observation is consistent with the solidification observed when attempting to pipette these liquids. This observation also confirms the detailed simulations and theoretical models of Melrose and co-workers,[6,23] who determined that true, hard-sphere dispersions will ''jam'' when shear thickened and cease to flow. The analysis of gap effects on shear thickening rheology further emphasizes that shear thickening is controlled by the applied shear *stress* and not shear rate, as the sample ceases to flow upon
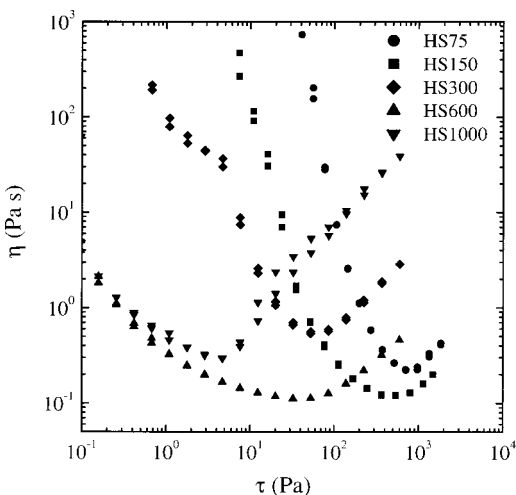
FIG. 6. Viscosity curves, corrected for secondary flows, for dispersions with various particle sizes at $\phi = 0.50$.

FIG. 8. Critical shear stress for shear thickening as a function of volume fraction for the various dispersions employed in the investigation.

strong shear thickening, and yet, can be readily made to flow by reducing the applied stress.

Figure 6 illustrates the effects of particle size on the dispersion rheology at fixed volume fraction. The flow curves systematically shift to lower shear stresses with increasing particle size, which can partially be accounted for by scaling the shear stress by the Brownian stress $\tau a^3 / k_B T$. However, this scaling fails to account for the variations in the minimums of the viscosity curves. Instead, these variations appear to be influenced by the magnitude of the electrostatic charge. Observe, that the minimum of the viscosity tends to decrease with increasing electrostatic charge as can be seen by comparing Fig. 6 with the zeta potentials tabulated in Table I.

Figure 7 provides another illustration of the effects of the electrostatics on the rheology by plotting the apparent zero shear viscosity as a function of the ratio of the volume fraction to the maximum packing volume fraction. The ap-

FIG. 7. Zero shear viscosity data as a function of reduced volume fraction (ϕ / ϕ_{max}) for the dispersions employed in this investigation. The line is the Krieger–Dougherty equation for reference. The values of ϕ_{max} are listed in Table I.
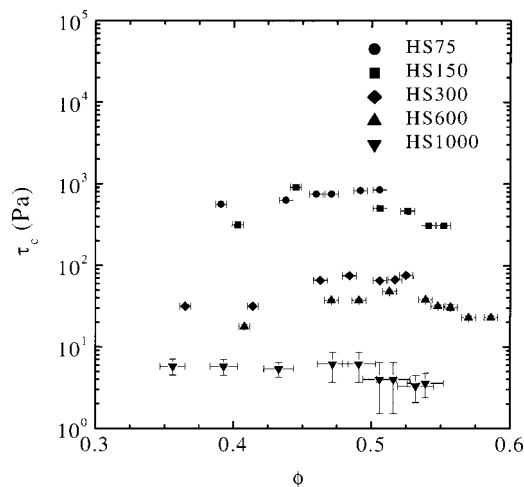
parent zero shear viscosity data for all the dispersions can be fit to a Krieger–Dougherty form [Eq. (4)]. The maximum packing volume fractions extracted from this data reduction are listed in Table I. The trend in the maximum packing volume fraction for the dispersions follows the same trend as $1/\kappa a$ for the dispersions. Note, that κa is only weakly dependent on volume fraction due to the background ionic strength. The dimensionless ratio of the Debye screening length to the particle radius, $1/\kappa a$, signifies the fractional increase in the effective radius of the particle due to the ion double-layer surrounding the charged particle, as per Eq. (3). Values of the parameter α are also given in Table I, and are comparable to those determined for other, concentrated, charge stabilized dispersions.[33] These values of α correspond to the approximate separation distance at which the potential is $1\ k_B T$. Thus, the zero shear viscosity results further confirm the important influence of the relatively weak, short range electrostatic interactions at high particle concentrations.

Each dispersion was examined in similar rheological detail and the onset of shear thickening identified from a double logarithmic plot of the data corrected for the effects of secondary flow. Figure 8 summarizes the critical shear stresses for shear thickening as a function of volume fraction for the monodisperse suspensions. The critical shear stress increase systematically with decreasing particle size. However, the critical shear stress is relatively insensitive to volume fraction whereas the critical shear rate is observed to decrease strongly with increasing volume fraction.

As noted previously,[13] shear thickening in these dispersions is governed by the applied stress. Previous authors have tried to correlate the dependence of the critical rate for shear thickening on particle size with limited success.[5,16] Here, we simply plot the measured critical stress vs the particle size for our homologous series of chemically similar particles. As shown in Fig. 9, a power law regression yields a dependence of $a^{-2.11 \pm 0.16}$. Although there is substantial scatter in this plot, a power law plot of the critical shear *rate* with size, such as has been proposed[5,16,20] is not viable due to the strong volume fraction, as well as size, dependence. As
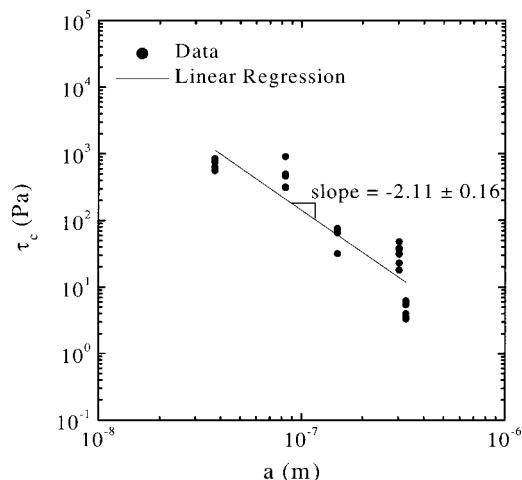
FIG. 9. Critical shear stress plotted against particle radius for all the dispersions at all concentrations. The line is a power law regression with slope of -2.11 ± 0.16.

FIG. 11. Critical shear stress for shear thickening as a function of volume fraction for various bimodal suspensions.

will be shown shortly, explicit consideration of the role of the interparticle potential on the onset of shear thickening is necessary to understand the behavior evident in these plots.

Figure 10 displays representative flow curves for a series of bimodal mixtures, as achieved by bimodal mixing of the afore mentioned dispersions, at fixed total volume fraction ($\phi = 0.53$). At low shear rates, the effects of mixing reduces the viscosity, which can be understood qualitatively in terms of an increase in the maximum packing fraction and the Krieger–Dougherty equation.[59] At higher shear rates, the mixtures are observed to shear thicken at critical stresses that lie between those defined by the pure component dispersions. A similar result was reported by D'Haene and Mewis,[60] and Bender and Wagner.[13] As also noted therein, mixing of particle sizes can lead to a less severe shear thickening transition. Note also that such mixtures would preclude the packing required for the order–disorder transition required by the analyses of Hoffman[19] and Boersma et al.[5]

Figure 11 illustrates the dependence of the critical shear stress on polydispersity by plotting the critical stress as a function of volume fraction for various bimodal dispersions. For reference the critical stress values for the monodisperse HS300 and HS1000 dispersions are include in Fig. 11. The critical stresses measured for the bimodal suspensions of the HS300 and HS1000 lie between the values for the monodisperse suspensions. The increase in polydispersity obtained with the bimodal suspensions decreases the suspension viscosity and the severity of the shear thickening and hence, the effects of shear thickening become unobservable at volume fractions higher than either of the monodisperse components. For example, shear thickening in the 1:1-HS300:HS1000 bimodal dispersions becomes immeasurable at volume fractions below 0.44, whereas shear thickening for the pure HS300 dispersion is apparent to volume fractions to 0.37. This is consistent with the increase in maximum packing fraction upon mixing.

For comparison and completeness, the scaling proposed by Bender and Wagner,[13] where the hydrodynamic and Brownian forces are proposed to be in balance, is applied to the data. The results of this scaling are shown in Fig. 12. Two important results are evident from this analysis. First, the magnitude of the reduced critical stress is of order 100, not of order one as would be expected if the forces were actually in balance. Second, the reduced critical stress is not observed to collapse to a common value across all data sets, showing that the $1/a^3$ Brownian scaling alone does not suffice. Closer examination of the plot, however, shows that some of the data sets do appear to reduce to a common value of approximately 300. The greatest deviations are seen for the samples with either high surface potentials or low values of κa. This is evidence that the electrostatic interactions must be accounted for in the force balance. Note that in the previous work[13] similar particles of a more restricted size and volume fraction range were examined. This scaling was sufficient to collapse this smaller data set, but with values still of order 10 for the dimensionless critical stress. The
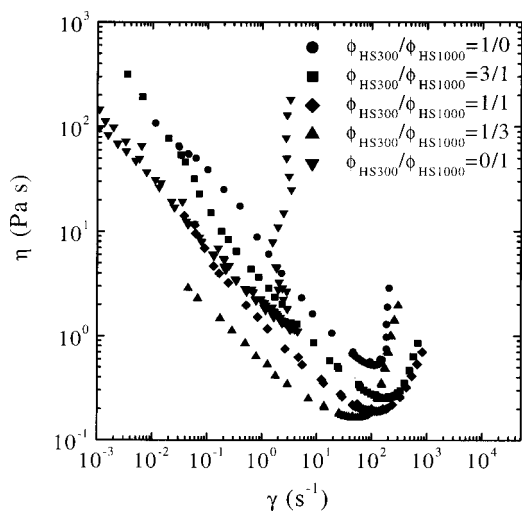

FIG. 10. Steady state viscosity curves for the bimodal suspensions of HS300 and HS1000 at various mixing ratios as indicated and constant volume fraction (0.53). Each curve is comprised of both ascending and descending stress.
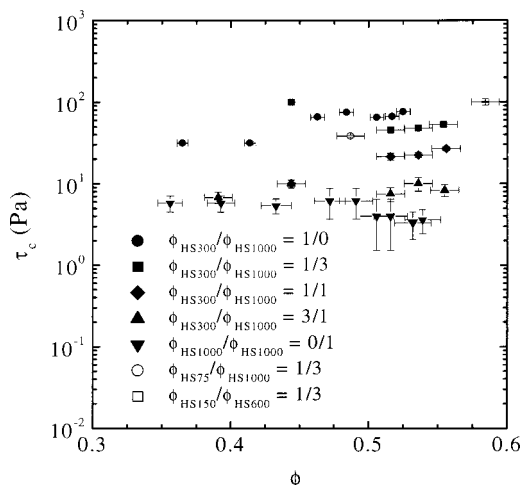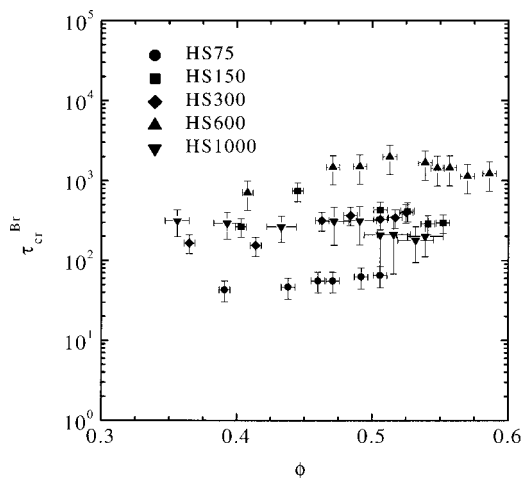
FIG. 12. Dimensionless critical shear stress as a function of volume fraction for the various dispersions employed in this investigation. The scaling is based on the balance of hydrodynamic and Brownian forces at the critical shear stress for shear thickening.
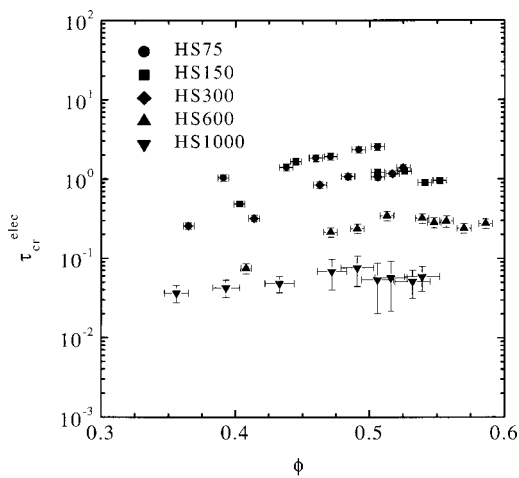

FIG. 13. Dimensionless critical shear stress as a function of volume fraction for the various dispersions employed in this investigation. The scaling is based on the proposal by Boersma et al. of a hydrodynamic and electrostatic force balance at the critical shear rate and supplemented with mean-field correction proposed by Bender and Wagner.

more extensive data set presented here shows that this scaling is not sufficient to correlate the onset of shear thickening for these near hard-sphere dispersions.

Comparison to the proposed scaling of (Ref. 5), which considers the electrostatic interactions to dominate, yields dimensionless critical shear rate. This scaling is found not to reduce the measured data for the critical shear rate, but rather exhibits a strong, systematic decrease in the critical Peclet number with increasing volume fraction and particle size. Further, the values are all orders of magnitude below that expected (of order one). As all of the parameters required in the analysis are accurately and independently measured and verified, these systematic deviations indicate that the proposed scaling for the critical shear rate does not contain the correct model for the onset of shear thickening. This also demonstrates that on a well defined, chemically similar set of particles of varying size, Barnes'[16] proposed $1/a^2$ scaling for the critical shear rate is not observed.

The volume fraction dependence evident in the critical shear rate can be largely accounted for by the mean-field correction.[13] Adopting the viewpoint that shear thickening is a consequence of hydrocluster formation results in the dimensionless critical stress given by Eq. (8). The data is plotted according to this reduction in Fig. 13. This reduction of the critical stress for shear thickening is now closer to the expected order and nearly independent of volume fraction, but as noted above, fails to account for the strong effects of particle size.

As the force balance approach is not sufficient to estimate the onset of shear thickening, we consider the argument of Chow and Zukoski[15] and Melrose and Ball,[23] which sets a criterion on the dynamics of the hydrocluster formation and relaxation under flow. A similar balance between the hydrodynamic and electrostatic forces is used to set the characteristic separation distance [Eq. (12)]. Calculations of the ratio of convection to relaxation time [Eq. (11)] yields a dimensionless critical shear rate. The results of this analysis are shown in Fig. 14.

The separation distance, h_m/a is plotted in the inset and compared to Eq. (6). The force balance of Melrose and Ball results in a closer approach that is less dependent on particle concentration, which is more physical than the simple geometric argument [Eq. (6)].

Although, this scaling collapses the data from different particle sizes reasonably well, a strong volume fraction dependence is still evident. Within the framework of this approach, a suspension should not shear thicken until the dimensionless shear rate is greater than one, i.e., $Pe_{cr}^M \geqslant 1$, which clearly is not satisfied. This deviation, which is not seen in the simulations can be traced to the retarding effects of many-body hydrodynamics on the relative particle motion, and hence, the slowing down of the hydrocluster relaxation (which are neglected in the simulations). Applying the
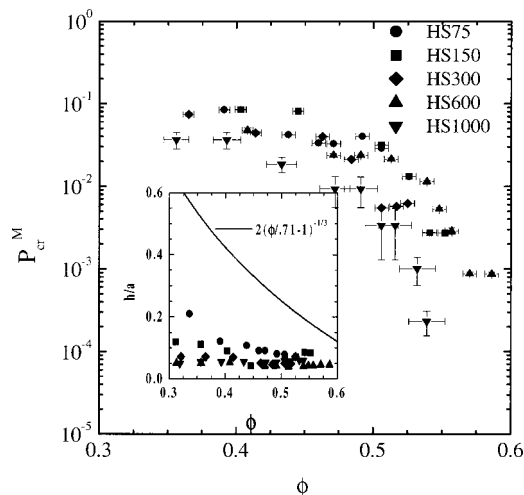

FIG. 14. Dimensionless critical shear rate as a function of volume fraction for the various dispersions employed in this investigation. The scaling is based on the proposal by Melrose and Ball. The inset plot shows the values of the calculated surface-to-surface separation as compared to the geometric ansatz.
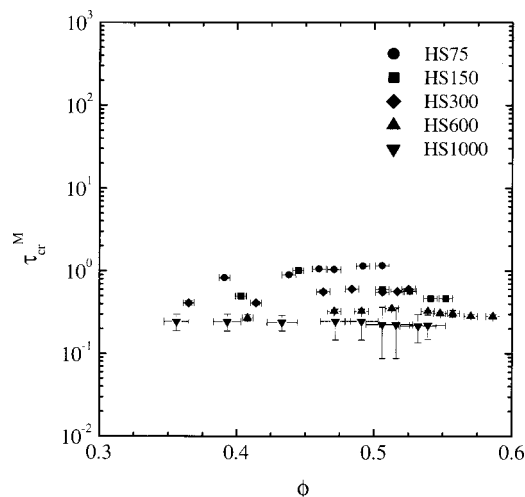
FIG. 15. Dimensionless critical shear stress as a function of volume fraction for the various dispersions employed in this investigation. The scaling is based on the proposal by Melrose and Ball corrected for many-body hydrodynamic interactions.
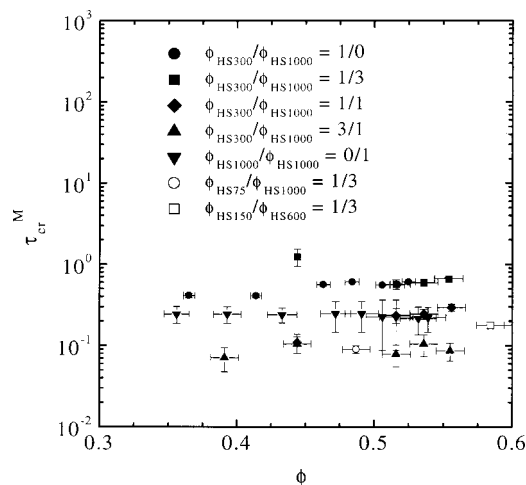

FIG. 16. Dimensionless critical shear stress as a function of volume fraction for various bimodal dispersions employed in this investigation. The scaling is based on the dynamic balance proposed by Melrose and Ball (Ref. 23) with the mean-field many-body hydrodynamic correction.

mean field correction for the many-body hydrodynamic interactions results in the reduction to the *critical stress* for shear thickening, given in shown in Fig. 15.

Clearly, this scaling analysis nearly collapses the data to a volume fraction independent constant of order one. There is a weak, systematic residual dependence on particle size, which accounts for part of the observed scatter. Although the nonlinearity of the equations does not enable extracting a simple powerlaw size dependence, comparison with Fig. 9 indicates that the critical stress must scale approximately with inverse particle size squared to successfully reduce the data.

This scaling analysis provides the only acceptable reduction of the experimental data. A critical test of this scaling is achieved by applying it to the measurements on two different sets of bimodal dispersion rheology. In this analysis the average particle radius, surface potential, and Debye length are simply calculated as number averages from the monodisperse disperse suspensions. Figure 16 shows the results of extending this new analysis to the bimodal suspensions. Again the scaling analysis performs well in reducing the data, and yields a dimensionless critical shear stress of order one. Thus, the scaling procedure provides an accurate procedure for predicting the critical shear stress for polydisperse suspensions in addition to monodisperse suspensions.

Finally, we note that the modified analysis proposed here provides a method to actually calculate the onset of shear thickening, not just a method to correlate existing data. Equations (12) and (13) are a closed set that can be solved simultaneously for the mean separation distance and critical shear stress at the point of shear thickening (where $\tau_{cr}^M \approx 1$). Note that, in agreement with theory, this analysis does not predict a lower critical volume fraction for hydrocluster formation and shear thickening (although the extent or severity of the shear thickening is not specified).

V. CONCLUSIONS

Measurements of reversible shear thickening over a broad range of model, near hard-sphere Stöber silica dispersions of varying particle size, but of the same chemistry, as well as bimodal mixtures of these particles, provide evidence for the hydrocluster mechanism of shear thickening. Characterization of the interparticle interactions indicates that despite coating with a silanol coupling agent, residual, unreacted surface silanol groups lead to short range electrostatic interactions that are shown to strongly influence the rheology of highly concentrated dispersions in a polar, index matching organic solvent. Analysis of the gap dependence in the shear thickened state indicates that severe shear thickening results in ''jamming'' such that the sample solidifies and slips, in agreement with simulations that account accurately for lubrication hydrodynamics. There is no evidence for a lower volume fraction for shear thickening; however the severity of the shear thickening is greatly suppressed as the volume fraction is reduced and secondary flows prevent accurate measurement of the weak thickening observed in Stokesian dynamics simulations of dilute, hard sphere dispersions.

The data for the onset of shear thickening and the analyses of that data within the framework of various models for the phenomena establish that shear thickening is stress controlled and that electrostatic repulsion plays a dominant role in determining the onset of shear thickening in these dispersions. Previous proposals for reducing the data based solely on force balances fail to reduce this data set. Accounting of the dynamics of the hydroclustered state leads to an improved and robust method for scaling the experimental data. As shown, proper accounting for the many-body hydrodynamic interactions is essential to reduce data across a broad range of particle concentrations, which can be accomplished to first order by a mean-field correction. Introducing this correction for suspension concentration into the dynamic scaling proposed by Melrose and Ball provides a robust reduction of the experimental data for both monodisperse and polydisperse (bimodal) dispersions. Further, these equations can be

used to predict the onset of thickening directly from knowledge of the physicochemical properties of the dispersion.

ACKNOWLEDGMENTS

APPENDIX: DERIVATION OF THE FORCE BALANCE MODELS

The scaling argument of Bender and Wagner[13] follows a similar derivation as presented earlier by Boersma et al.,[5] whereby a force balance between two particles is considered at the point of shear thickening. Although similar in final form, the conceptual picture underlying the two models is very different; Boersma et al. consider the forces required to rotate two particles out of a flow-aligned ordered microstructure aligned along the flow planes in laminar shear (i.e., Hoffman's proposal[19]), while Bender and Wagner considered the conditions necessary for hydrodynamic lubrication forces to determine the colloidal microstructure in a laminar shear flow. Both derivations start by estimating the hydrodynamic force acting between a particle pair in a Newtonian solvent in a laminar shear flow. The particles are placed in the plane of shear and aligned along the compression axis (135° relative to the shear direction). The force required to drive two particles together along the line of centers is given (for a Newtonian solvent) by standard expressions.[48,61] An asymptotic form valid for small gaps in the lubrication approximation is given explicitly by Melrose and co-workers [see Ref. 62, Eq. (1)]. This resistance coefficient scales with the Stokes drag, which is proportional to the particle size and the solvent viscosity, and the relative velocity, which is proportional to the applied shear rate. Further, the force required to move a particle in the close presence of another particle must be mofidied to account for the strong squeezing flow between particle surfaces, which scales as a/h, with $h = r - 2a$ the surface-to-surface separation distance. Thus, the asymptotic force required to squeeze particles together in laminar shear is

$$F_{\text{hydrodynamic}} \approx 3\pi\mu a^3 \dot{\gamma}/2h.$$

This value is a factor of 4 less than that assumed by Boersma et al. and a factor of 2 less than that of Bender and Wagner.

In a concentrated dispersion, many-body hydrodynamic interactions must be accounted for. To first order, the particle pair can be thought of as being embedded in an effective medium, with a viscosity given by the viscosity due to all hydrodynamic interactions in the concentrated dispersion. This viscosity is taken to be that of the dispersion to first order. Multiplying the above expression by the relative suspension viscosity (which is a function of shear rate) yields an expression for the hydrodynamic force acting on the pair in terms of the applied shear stress, which is the product of the suspension viscosity and shear rate,

$$F_{\text{hydrodynamic}} \approx 3\pi a^3 \tau/2h.$$

Note that this approximation does not suppose the lubrication force itself acts through the effective medium, for it surely acts through the solvent. Rather the correction recognizes that the force acting to compress the pair along the compression axis is not the solvent viscosity times the shear rate, but rather, the total hydrodynamic viscosity times the shear rate. For high shear rates prior to shear thickening, the suspension viscosity is approximately the hydrodynamic viscosity.[2,13,27] Further discussion of this mean-field approximation, its successful application, and other variations of hydrodynamic preaveraging can be found in Refs. 45, 49–51.

The ratio of this force to the dominant repulsive force, which for Brownian hard spheres is given by the statistical expression of Batchelor,[39] $F_{\text{Brownian}} = -kT[\partial \ln g(r)/\partial r]$ should be of order one at the applied shear stress when hydroclusters form and shear thickening is evident. This ratio is given in Eq. (5). This balance is readily generalized to include interparticle forces, such as repulsive interactions as considered by Boersma et al. Finally, it is essential to specify the viscosity at the shear thickening point if one wishes to calculate the shear rate for the onset of shear thickening. In this case robust correlations for hard-sphere viscosity[49,51,63] can be applied.[13]

[1] P. D'Haene, J. Mewis, and G. G. Fuller, J. Colloid Interface Sci. **156**, 350 (1993).
[2] J. W. Bender and N. J. Wagner, J. Colloid Interface Sci. **172**, 171 (1995).
[3] B. Kaffashi, V. T. OBrien, M. E. Mackay, and S. M. Underwood, J. Colloid Interface Sci. **181**, 22 (1997).
[4] G. Bossis and J. F. Brady, J. Chem. Phys. **91**, 1866 (1989).
[5] W. H. Boersma, J. Laven, and H. N. Stein, AIChE J. **36**, 321 (1990).
[6] R. S. Farr, J. R. Melrose, and R. C. Ball, Phys. Rev. E **55**, 7203 (1997).
[7] L. E. Silbert, J. R. Melrose, and R. C. Ball, Mol. Phys. **96**, 1667 (1999).
[8] T. N. Phung and J. F. Brady, J. Fluid Mech. **313**, 181 (1996).
[9] J. F. Brady, Curr. Opin. Colloid Interface Sci. **1**, 472 (1996).
[10] M. C. Newstein, H. Wang, N. P. Balsara, A. A. Lefebvre, Y. Shnidman, H. Watanabe, K. Osaki, T. Shikata, H. Niwa, and Y. Morishima, J. Chem. Phys. **111**, 4827 (1999).
[11] H. M. Laun, R. Bung, S. Hess, W. Loose, O. Hess, K. Hahn, E. Hadicke, R. Hingmann, F. Schmidt, and P. Lindner, J. Rheol. **36**, 743 (1992).
[12] W. J. Frith, P. d'Haene, R. Buscall, and J. Mewis, J. Rheol. **40**, 531 (1996).
[13] J. W. Bender and N. J. Wagner, J. Rheol. **40**, 899 (1996).
[14] R. L. Hoffmann, Trans. Soc. Rheol. **16**, 155 (1972).
[15] M. K. Chow and C. F. Zukoski, J. Rheol. **39**, 33 (1995).
[16] H. A. Barnes, J. Rheol. **33**, 329 (1989).
[17] I. Wagstaff and C. E. Chaffey, J. Colloid Interface Sci. **59**, 53 (1977).
[18] G. B. Franks, Z. Zhou, N. J. Duin, and D. V. Boger, J. Rheol. **44**, 759 (2000).
[19] R. L. Hoffmann, J. Colloid Interface Sci. **46**, 491 (1972).
[20] R. L. Hoffmann, J. Rheol. **42**, 111 (1998).
[21] J. F. Brady and G. Bossis, Annu. Rev. Phys. Chem. **20**, 111 (1988).
[22] A. A. Catherall, J. R. Melrose, and R. C. Ball, J. Rheol. **44**, 1 (2000).
[23] J. R. Melrose and R. C. Ball, Proceedings of the XIIIth International Congress of Rheology, British Society of Radiology **2**, 421 (2000).
[24] M. K. Chow and C. F. Zukoski, J. Rheol. **39**, 15 (1995).
[25] H. M. Laun, R. Bung, and F. Schmidt, J. Rheol. **35**, 999 (1991).
[26] R. J. Butera, M. S. Wolfe, J. Bender, and N. J. Wagner, Phys. Rev. Lett. **77**, 2117 (1996).
[27] V. T. OBrien and M. E. Mackay, Langmuir **16**, 7931 (2000).
[28] D. I. Dratler, W. R. Schowater, and R. L. Hoffman, J. Fluid Mech. **353**, 1 (1997).

[29] A. P. Philipse and A. Vrij, J. Colloid Interface Sci. **128**, 121 (1988).

[30] A. van Blaaderen, J. van Geest, and A. Vrij, J. Colloid Interface Sci. **154**, 481 (1992).

[31] A. van Blaaderen and A. Vrij, J. Colloid Interface Sci. **156**, 1 (1993).

[32] B. J. Maranzano, N. J. Wagner, G. Fritz, and O. Glatter, Langmuir **16**, 10556 (2000).

[33] N. J. Wagner, R. Krause, A. R. Rennie, B. D'Aguanno, and J. Goodwin, J. Chem. Phys. **95**, 494 (1991).

[34] J. W. Bender, ''*Rheo-optical Investigations of the Microstructure of Model Colloidal Suspension*,'' Ph.D. thesis, University of Delaware, 1995.

[35] C. G. de Kruif, E. M. F. VanLersel, A. Vrij, and W. B. Russel, J. Chem. Phys. **83**, 4717 (1985).

[36] J. C. van der Werff and C. G. de Kruif, J. Rheol. **33**, 421 (1989).

[37] C. J. Rueb and C. F. Zukoski, J. Rheol. **42**, 1451 (1998).

[38] I. Bodnar, A. Silva, R. W. Deitcher, N. E. Weisman, N. J. Wagner, and Y. H. Kim, J. Polym. Sci., Part B: Polym. Phys. **38**, 857 (2000).

[39] G. K. Batchelor, J. Fluid Mech. **83**, 97 (1977).

[40] J. Bergenholtz and N. J. Wagner, Ind. Eng. Chem. Res. **33**, 2391 (1994).

[41] C. W. Macosko, *Rheology Principles, Measurements, and Applications* (Wiley–VCH, New York, 1994).

[42] G. Hay, M. E. Mackay, S. A. McGlashan, and Y. S. Park, J. Non-Newtonian Fluid Mech. **92**, 187 (2000).

[43] W. B. Russel and M. C. Grant, Colloids Surf., A **161**, 271 (2000).

[44] J. C. van der Werff, C. G. de Kruif, and J. K. G. Dhont, Physica A **160**, 195 (1989).

[45] B. J. Maranzano and N. J. Wagner, Rheol. Acta **39**, 483 (2000).

[46] F. M. Horn, W. Richtering, J. Bergenholtz, N. Willenbacher, and N. J. Wagner, J. Colloid Interface Sci. **225**, 166 (2000).

[47] I. M. Krieger and T. J. Dougherty, Trans. Soc. Rheol. **3**, 137 (1959).

[48] W. B. Russel, D. A. Saville, and W. R. Schowalter, *Colloidal Dispersions* (Cambridge University Press, Cambridge, 1989).

[49] J. F. Brady, J. Chem. Phys. **99**, 567 (1993).

[50] S. R. Rastogi and N. J. Wagner, J. Rheol. **41**, 893 (1997).

[51] R. A. Lionberger and W. B. Russel, J. Rheol. **41**, 399 (1997).

[52] O. Glatter, J. Appl. Crystallogr. **30**, 431 (1977).

[53] B. J. Maranzano and N. J. Wagner, J. Chem. Phys. (to be submitted).

[54] A. van Blaaderen and A. P. M. Kentgens, J. Non-Cryst. Solids **149**, 161 (1992).

[55] J. F. Brady and J. F. Morris, J. Fluid Mech. **348**, 103 (1997).

[56] D. R. Foss and J. F. Brady, J. Fluid Mech. **407**, 167 (2000).

[57] A. Yoshimura and R. K. Prud'homme, J. Rheol. **32**, 53 (1988).

[58] D. J. Henson and M. E. Mackay, J. Rheol. **39**, 359 (1995).

[59] D. Quemada, Eur. Phys. J.: Appl. Phys. **1**, 119 (1998).

[60] J. Mewis and P. D'Haene, Makromol. Chem., Macromol. Symp. **68**, 313 (1993).

[61] G. K. Batchelor and J. T. Green, J. Fluid Mech. **56**, 401 (1972).

[62] J. R. Melrose, J. H. van Vliet, and R. C. Ball, Phys. Rev. Lett. **77**, 4660 (1996).

[63] J. Bergenholtz, F. M. Horn, W. Richtering, N. Willenbacher, and N. J. Wagner, Phys. Rev. E **58**, 4088 (1998).